FEDSM2012-72219

OPTIMAL PERTURBATIONS IN BOUNDARY LAYER FLOWS
OVER ROUGH SURFACES

S. Cherubini[*]

Dipartimento di Ingegneria Meccanica e Gestionale,
DIMeG, CEMeC
Politecnico di Bari
Bari, Italy
Email: s.cherubini@gmail.com

M. D. de Tullio
P. De Palma
G. Pascazio
Dipartimento di Ingegneria Meccanica e Gestionale
DIMeG, CEMeC
Politecnico di Bari
Bari, Italy
Email: m.detullio@poliba.it,
depalma@poliba.it, pascazio@poliba.it

ABSTRACT

This work provides a three-dimensional energy optimization analysis, looking for perturbations inducing the largest energy growth at a finite time in a boundary-layer flow in the presence of roughness elements. Amplification mechanisms are described which by-pass the asymptotical growth of Tollmien–Schlichting waves. The immersed boundary technique has been coupled with a Lagrangian optimization in a three-dimensional framework. Two types of roughness elements have been studied, characterized by a different height. The results show that even very small roughness elements, inducing only a weak deformation of the base flow, can strongly localize the optimal disturbance. Moreover, the highest value of the energy gain is obtained for a varicose perturbation, pointing out the importance of varicose instabilities for such a flow and a different behavior with respect to the secondary instability theory of boundary layer streaks.

INTRODUCTION

Transition to turbulence in spatially developing boundary-layer flows is a fundamental issue for many aerodynamic and industrial applications, such as airplane wings and gas turbine blades. In fact, in these cases, the performance of the components, in terms of loss coefficient or drag coefficient, as well as

the control of the flow at different operating conditions, strongly depend on the nature (laminar or turbulent) of the boundary layer. For instance, on commercial aircraft about 50% of the total drag is due to the turbulent skin-friction associated with the boundary layers, and about 90% for submarines [1]. Nevertheless, an accurate prediction of boundary-layer transition is still not possible, and further fundamental knowledge is needed to develop accurate prediction models of engineering interest [2, 3]. Nowadays it is well–known that transition is triggered by exogenous disturbances, namely wall roughness, acoustic waves, or freestream turbulence, but the understanding of the transition mechanism is still an open problem. For small amplitude disturbances and supercritical Reynolds numbers, the linear stability analysis predicts the slow transition process due to the generation, amplification and secondary instability of Tollmien–Schlichting (TS) waves [4]. However, even if the regime is subcritical (i.e. all eigenmodes are damped), there exist some disturbances which could induce a transient amplification. Transient growth arises from the constructive interference of damped non-orthogonal eigenmodes and results in a spatial amplification of the disturbances [4]. If growth is sufficient, such amplified structures could induce secondary instability and breakdown, leading to a by-pass transition (see [5, 6]).

With the aim of analysing the early phases of bypass transition, the concept of "optimal perturbation" was introduced (see [7, 8]),

---

[*]Address all correspondence to this author.

which is defined as the perturbation of the steady base flow able to induce the maximum energy growth at a target time. Since then, many works have focused on the "local" stability analysis of parallel and weakly non-parallel flows, looking for "local optimal perturbations" characterized by a given wavenumber in the streamwise and spanwise direction [9–13]. In a boundary layer, the optimal perturbation has been found to be characterized by a counter-rotating vortex pair without any modulation in the streamwise direction, and resulting at finite time in a pair of streamwise velocity streaks. The results of such an analysis are very promising, but the drawbacks of such "local" methods are that they focus onto a single wavenumber/frequency and that they neglect the effects due to the non-parallelism of the flow.

In the past few years, these limitations have been overtaken thanks to the development of the "global" stability analysis, which considers two (or three) eigendirections, allowing to study a non-parallel base flow with general perturbations (not a single wavenumber) [14–16]. The global approach allows to take into account the transient amplification of the disturbance energy due to the non-orthogonality of the eigenvectors, providing a useful tool to study the early phases of by-pass transition (for the case of the boundary-layer flow, see [17]).

Although much progress has been made in the study of transition in boundary-layer flows, the process by which surface roughness affects the laminar-turbulent transition is not well understood. Pioneer work in this field has been performed experimentally by Acalar and Smith [18], and numerically by Joslin and Grosch [19]. Such studies have identified a vortex generation and shedding mechanism, which completely bypasses the linear instability process. In fact, the presence of the roughness has been found to affect the receptivity of the boundary layer with respect to external disturbances, modifying the asymptotical and transient mechanisms governing the flow. The flow around isolated three-dimensional bumps has been studied both theoretically and numerically (see [19, 20]), showing the existence of a complex pattern of streamwise streaks and vortices, similar to the optimal disturbances affecting a boundary-layer on a flat plate. Many experimental and numerical works (see [21–23]) have focused on the effects of these roughness-induced streaks on the growth of TS waves, showing that streaks of a certain amplitude could induce the stabilization of unstable TS waves. Very recently, these results have been theoretically validated by a two-dimensional global analysis of the flow past a three-dimensional bump (see [24]), assessing the stabilizing effect of a pre-streaky flow on the growth of TS waves. The aim of the present work is to assess whether the roughness elements are capable of inducing three-dimensional amplification mechanisms which by-pass the two-dimensional asymptotical growth and lead the flow to transition even if the TS waves are stable. To this purpose, we perform a fully three-dimensional energy optimization analysis, looking for perturbations inducing the largest energy growth at a finite time in a boundary-layer flow in the presence of a three-

dimensional bump. The shape of the roughness element has been described by the immersed boundary (IB) technique, useful to handle complex geometries, already employed for the stability analysis of the two-dimensional flow past a cylinder in [25].

The paper is organized as follows. In the second section we define the problem and describe the optimization method as well as the IB technique. In the third section, a thorough discussion of the results of the optimization analysis is provided. Finally, concluding remarks are provided.

PROBLEM FORMULATION
Governing equations and numerical method

The behavior of a three-dimensional incompressible flow is described by the following governing equations:

$$\mathbf{u}_t + (\mathbf{u} \cdot \triangledown)\mathbf{u} = -\triangledown p + \frac{1}{Re}\triangledown^2 \mathbf{u} \qquad (1)$$

$$\nabla \cdot \mathbf{u} = 0 \qquad (2)$$

where $\mathbf{u}$ is the velocity vector and p is the pressure term (including the contribution of conservative-force fields). Dimensionless variables are defined with respect to the Blasius boundary-layer displacement thickness at the center of the roughness element, δ^*, and the freestream velocity, U_∞, so that the Reynolds number is $Re = U_\infty \delta^*/\nu$, ν being the kinematic viscosity. The roughness element is an axisymmetric bump and its contour is defined by $h(x,z) = h_0 cos^3(\pi r/d)$, where h_0 is the maximum height, r is the radial coordinate, and d is the diameter [24]. For the following computations we have used two values of h_0, namely, $h_0 = 0.75$, and $h_0 = 1.5$, whereas the diameter, $d = 26$, is kept constant. The computational domain has dimensions equal to $L_x = 216$, $L_y = 27.5$ and $L_z = 72$ x, y and z being the streamwise, wall-normal and spanwise directions, respectively. The roughness element is centered at $x = 77.5$, $z = 36$.

The base flow is obtained by integrating the Navier–Stokes equations with the following boundary conditions: at inlet points, placed at $x_{in} = 36$ downstream of the leading edge of the plate, the Blasius boundary-layer profile is imposed for the streamwise and wall-normal components of the velocity vector whereas the spanwise component is set to zero. At outlet points, a standard convective condition is employed [26]. In the spanwise direction periodicity is imposed for the three velocity components. At the upper-boundary points the Blasius solution is imposed for the wall-normal component of the velocity, whereas the spanwise velocity component and the spanwise vorticity are set to zero. Finally, at the bottom boundary the no-slip boundary condition is prescribed along the plate and the roughness element surface by using an IB technique, which is detailed in the next subsection. The governing equations are discretized by a finite-difference fractional-step method [27]. The viscous terms are
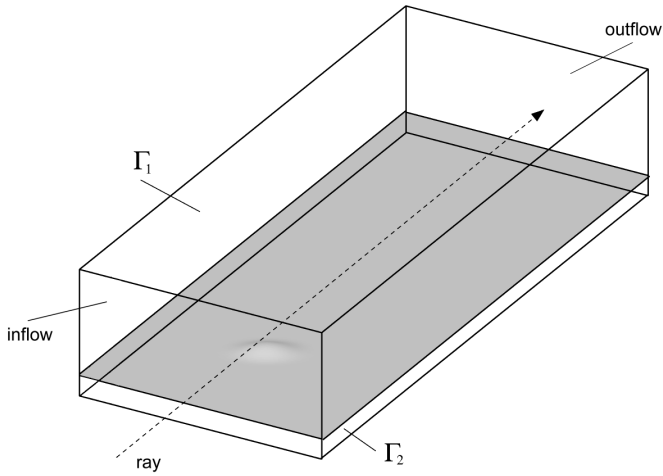
FIGURE 1. Sketch of the computational domain: Γ_1 and Γ_2 indicate the fluid and solid regions respectively, separated by the body surface, in gray.

discretized in time using an implicit Crank–Nicolson scheme, whereas an explicit third-order-accurate Runge–Kutta scheme is employed for the non-linear terms. A second-order-accurate centered space discretization is used on a staggered grid. After a grid-convergence analysis, a mesh made up by $301 \times 150 \times 91$ points is selected for the reference domain.

Immersed-boundary technique

The IB technique is employed to take into account the presence of a single or multiple bodies inside the computational domain, while maintaining the use of Cartesian grids, thus not conforming to the geometry surfaces. Being the volume grid (and therefore its resolution at the wall) independent of the geometry surface discretization, the surface description focus uniquely on resolving the geometry. In this work, the body surface is discretized by means of unconnected triangles of size inversely proportional to the local curvature of the original surface (STL format), with the only requirement that the object must be a closed manifold. The body surface is overlapped onto the volume mesh, splitting it in fluid and solid regions, Γ_1 and Γ_2, respectively, in figure 1. Note that the gray surface indicated in figure 1 is not a closed geometry. Indeed, in our implementation of the method, when the body intersects the boundaries of the computational domain, the domain boundary faces act as closure faces for the body.

In order to assign the computational cells to each zone, a tagging procedure is performed, finding their relative position with respect to the body. This is done automatically by using a very efficient ray-tracing technique [28], which consists in casting rays

in one Cartesian direction, spanning from a reference fluid point and counting the intersections with the body surface. The number of valid intersections will then classify the cells as fluid (even number of intersections) or solid (odd number of intersections). With reference to figure 1, in this work the rays are cast in the flow direction, starting for each point laying on the inlet surface. After the tagging, the fluid points that have at least one neighbor that is tagged as solid, are tagged as interface points. For these points, the shortest Cartesian distance with respect to the body surface is evaluated.

At every point of the computational domain $\Gamma_1 + \Gamma_2$, the governing equations (1) and (2) are solved. In the present work, the direct forcing of [29] is employed; therefore, at interface points a correction on the velocity value is forced at each time step so as to impose the desired velocity value on the body surface. Following [30], the velocity at the interface points is obtained by linearly interpolating the velocity at a second grid point (which is obtained by directly solving the Navier–Stokes equations) and the velocity at the body surface, which conceptually corresponds to applying the momentum forcing inside the flow field. For each interface point, the direction towards the second grid point, i.e. the interpolation direction, is the Cartesian direction in which the distance with respect to the body is minimum. This also identifies the body intersections. Concerning the solid points, the zero-velocity forcing is applied (stationary boundary). It is worth noting that, as checked by [30], for stationary boundary problems, different treatments inside the solid body do not affect the external flow. The present IB technique is coupled with the Lagrangian optimization described in the following.

Lagrangian optimization

The linear behavior of a perturbation $\mathbf{q} = (u', v', w', p')^T$ evolving in a laminar incompressible flow over a roughness element placed over a flat plate is studied by employing the governing equations linearized around the steady state $\mathbf{Q} = (U, V, W, P)^T$. A zero perturbation condition is chosen for the three velocity components at the x and y boundaries, whereas periodicity of the perturbation is imposed in the spanwise direction. The zero perturbation condition at the outflow is enforced by means of a fringe region, which allows the perturbation at the exit boundary to vanish smoothly.

In order to identify the perturbation at $t = 0$ which is able to produce the largest disturbance growth at any given target time, T, a Lagrange multiplier technique is used [31]. Let us define the disturbance energy as:

$$E(t) = \int_V \left(u'^2(t) + v'^2(t) + w'^2(t) \right) dV \qquad (3)$$

where V is the computational volume. The objective function of the procedure is the energy gain at the target time $t = T$, i.e.

3

$E(T)/E(0)$. The Lagrange multiplier technique consists in seeking extrema of the augmented functional $\mathscr{L}$ with respect to every independent variable. Such a functional is written as:

$$\mathscr{L} = \frac{E(T)}{E(0)} + \int_V \int_0^T a\left(u'_x + v'_y + w'_z\right) dt\,dV$$

$$+ \int_V \int_0^T b\left(u'_t + (u'U)_x + U_y v' + V u'_y + U_z w' + W u'_z\right.$$

$$\left. + p'_x - \frac{u'_{xx} + u'_{yy} + u'_{zz}}{Re}\right) dt\,dV$$

$$+ \int_V \int_0^T c\left(v'_t + U v'_x + (v'V)_y + u' V_x + V_z w' + W v'_z\right. \qquad (4)$$

$$\left. + p'_y - \frac{v'_{xx} + v'_{yy} + v'_{zz}}{Re}\right) dt\,dV$$

$$+ \int_V \int_0^T d\left(w'_t + U w'_x + V w'_y + W_x u' + W_y v' + (Ww')_z\right.$$

$$\left. + p'_z - \frac{w'_{xx} + w'_{yy} + w'_{zz}}{Re}\right) dt\,dV$$

where the linearized governing equations (direct problem) have been imposed as constraints, and a, b, c, d are Lagrange multipliers. Integrating by parts and setting to zero the first variation of $\mathscr{L}$ with respect to u', v', w', p' leads to the adjoint equations:

$$b_t = -b_x U - (bV)_y + cV_x - (bW)_z + W_x d - a_x - \frac{b_{xx} + b_{yy} + b_{zz}}{Re}$$

$$c_t = -(cU)_x - c_y V + bU_y - (cW)_z + W_y d - a_y - \frac{c_{xx} + c_{yy} + c_{zz}}{Re}$$

$$d_t = -(dU)_x - (dV)_y + U_z b + V_z c - W d_z - a_z - \frac{d_{xx} + d_{yy} + d_{zz}}{Re}$$

$$b_x + c_y + d_z = 0$$

$$\tag{5}$$

where $\mathbf{q}^\dagger = (a, b, c, d)^T$ is now identified as the adjoint vector. By using the boundary conditions of the direct problem, one obtains:

$$\begin{aligned} b = 0, c = 0, d = 0, &\text{ for } y = y_w \text{ and } y = L_y \\ b = 0, c = 0, d = 0, &\text{ for } x = x_{in} \text{ and } x = x_{out} \end{aligned} \qquad (6)$$

where the zero perturbation condition at the wall is imposed by means of the immersed boundary technique for both the direct and adjoint equations; it is noteworthy that, using the direct forcing approach, no explicit forcing term appears in the adjoint equations. Nullifying the terms at $t = T$ one obtains the compatibility conditions [31]:

$$\frac{2u'}{E(0)} - b = 0, \quad \frac{2v'}{E(0)} - c = 0, \quad \frac{2w'}{E(0)} - d = 0, \text{ for } t = T \quad (7)$$

By solving the direct and adjoint equations at each step of the iterative procedure, the first variation of the augmented functional with respect to $\mathbf{q}$ and $\mathbf{q}^\dagger$ is set to zero. Moreover, the gradient of $\mathscr{L}$ with respect to the initial state $\mathbf{q}_0$ has to vanish within a reasonable number of iterations. In order to achieve convergence efficiently, a conjugate gradient algorithm is used, similar to that employed in [32]. The initial state is updated in the steepest ascent direction, denoted as $\nabla_{\mathbf{q}_0}\mathscr{L}$, namely:

$$\frac{\partial \mathscr{L}}{\partial u'_0} = -2u'_0 \frac{E(T)}{E(0)^2} + b(0)$$

$$\frac{\partial \mathscr{L}}{\partial v'_0} = -2v'_0 \frac{E(T)}{E(0)^2} + c(0) \qquad (8)$$

$$\frac{\partial \mathscr{L}}{\partial w'_0} = -2w'_0 \frac{E(T)}{E(0)^2} + d(0)$$

with an adjustable step length α, so that $\mathbf{q}_0^{(n+1)} = \mathbf{q}_0^n + \alpha^n \nabla_{\mathbf{q}_0}\mathscr{L}^n$. After the first iteration in the steepest ascent direction, the successive steps are taken along a conjugate direction, $\Lambda\mathbf{q}_0$, which is computed on the basis of the gradient at two consecutive iterations according to $\Lambda\mathbf{q}_0^{(n+1)} = \nabla_{\mathbf{q}_0}\mathscr{L}^{(n+1)} + \beta^{(n+1)}\Lambda\mathbf{q}_0^n$. The value of the parameter $\beta^{(n+1)}$ is computed by means of the Polak–Ribière formula [33]. The step length α has been chosen small enough in order to ensure convergence to the optimal value.

The optimization procedure for a chosen target time T can be summarized as follows:

1. An initial guess is taken for the initial condition, q_0, at $t = 0$, with an associated initial energy $E(0)$.
2. The direct problem is integrated from $t = 0$ to $t = T$.
3. At $t = T$, the initial state for the adjoint problem is provided by the compatibility condition (7).
4. The adjoint problem (5) is integrated backward in time from $t = T$ to $t = 0$, starting from the initial state of step (3).
5. At $t = 0$, the initial direct state is updated in the direction of the conjugate gradient with step length α and β computed according to the Polak–Ribière formula ($\beta = 0$ is imposed at the first iteration).
6. The objective function $E(T)/E(0)$ is evaluated; if its increase between two successive iterations is smaller than a chosen threshold, $e = 10^{-5}$, the loop is stopped, otherwise the procedure is continued from step (2).

The performance of the optimization procedure, as well as a detailed convergence study for the case of the Blasius boundary-layer flow are provided in [17, 34].
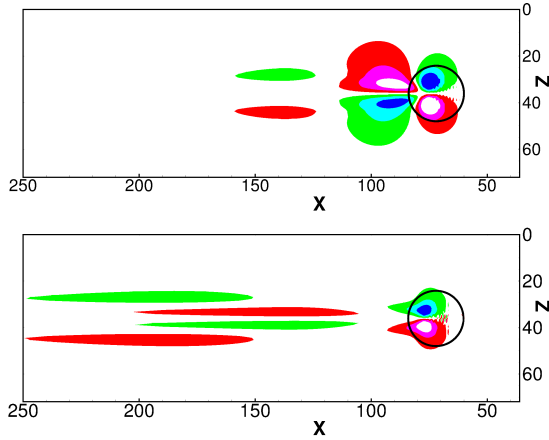
FIGURE 2. Contours of positive (red) and negative (green) streamwise vorticity in the plane $y = h_0 + 1$, for the two base flows with $h_0 = 0.75$ (upper frame), and $h_0 = 1.5$ (lower frame). The black circle represents the bump.
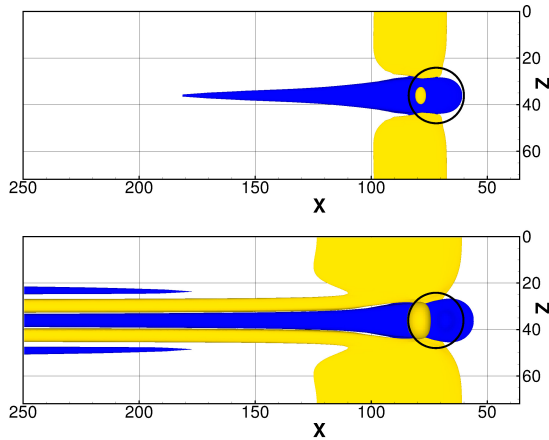

FIGURE 3. Surfaces of the positive (yellow) and negative (blue) deviation of the streamwise component of velocity with respect to the spanwise mean for the two base flows with $h_0 = 0.75$ (upper frame), and $h_0 = 1.5$ (lower frame). The black circle represents the bump.

RESULTS
Base flow

The steady base flow has been computed for $Re = 235$, using two bump heights, namely, $h_0 = 0.75$, and $h_0 = 1.5$. As found in previous works (see [19, 21, 24]), we observe counter-rotating vortices downstream of the roughness element, shown in Figure 2 which provides the streamwise vorticity in the plane $y = h_0 + 1$ for the two base flows. It is noteworthy that the larger bump induces elongated streamwise vortices with a large development in the streamwise direction, whereas the smallest one is charac-

terized by large vorticity regions in the near field downstream of the roughness element, mostly due to the wake of the bump. The streamwise vortices transport the high-speed fluid from the outer region of the boundary layer towards the wall, whereas the low-speed fluid is transported away from the wall. This results into streamwise streaks which can be visualized by subtracting to the streamwise component of velocity its mean value in the spanwise direction, $\overline{U}(x,y) = \frac{1}{L_z} \int U(x,y,z)dz$. The streamwise velocity deviation, $u(x,y,z) - \overline{U}(x,y)$, is provided in Figure 3 for the two base flows, showing the streamwise streaks developing into the boundary layer. One can notice that for the smallest bump the low- and high- momentum regions are localized close to the roughness element, whereas for the largest one the streaks strongly develop and amplify in the streamwise direction.

Optimal perturbations

Direct-adjoint optimizations have been performed for the two base flows described above. Figure 4 shows the value of the optimal energy gain versus the target time for the Blasius base flow (red circles), the smaller bump (green triangles), and the larger one (blue squares). One can observe that, in the presence of the roughness element, the energy gain is larger than the one obtained for the Blasius base flow, although for the smaller bump non negligible differences are obtained only at a large target time. Comparing the two cases with the roughness elements, the largest differences in energy gain are recovered at small times, the energy growth induced by the larger bump overtaking of one order of magnitude the energy growth induced by the smaller one. This indicates that different amplification mechanisms are recovered in the two cases, and that the largest the streak amplitude in the base flow, the strongest the transient growth of the energy.

The differences in the energy gain values correspond to different shapes and localizations of the initial optimal perturbations. Figures 5 (left) and 6 show the surfaces of the spanwise component of the initial optimal perturbation for the Blasius base flow, and for the smaller and the larger bumps (from left to right), respectively, at a small target time, $T = 50$. For the Blasius base flow, as already found by the global optimizations in [17, 35], the initial optimal perturbation is composed of upstream-inclined vortices, aligned with the $x-$axis, but alternated in the streamwise and spanwise direction. Since the Blasius flow is homogeneous in the spanwise direction, the result of the optimization contains only one wavenumber in that direction, β, namely the one able to induce the largest amplification among the multiples of the spanwise minimum wave number, $\beta_L = (2\pi)/L_z$, which is the minimum one allowed in the considered domain. The spanwise wavenumber of the optimal perturbation obtained at $T = 50$ is $\beta = 0.87$; this wavenumber slightly decreases for larger target times, reaching at the optimal time a value which is close to the optimal wave number computed locally by [13], namely, $\beta = 0.6$.
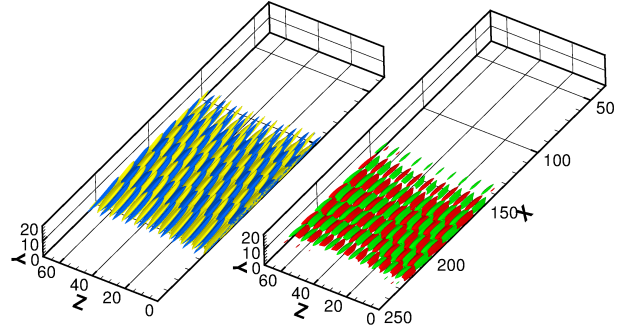
FIGURE 5. Iso-surfaces of the spanwise component of velocity (blue and yellow for negative and positive values, respectively) of the initial optimal perturbation (left) obtained at $T = 50$, and of the streamwise one (green and red for negative and positive values, respectively) of the optimal perturbation at $t = T$ (right), for the Blasius base flow.

FIGURE 4. Optimal energy gain versus target time for the Blasius base flow (red circles) and for the base flows in the presence of the smallest (green triangles) and the largest bump (blue squares).

In the presence of the roughness element, the base flow is not homogeneous in the spanwise direction, so the optimal perturbation do not show only one wavenumber β. Indeed, the optimal disturbance is localized in the small spanwise zone where the bump is placed, being composed of pairs of upstream-inclined vortices, aligned with the $x-$axis, alternated in the spanwise and streamwise direction, and characterized by a dominant spanwise wavelength which is slightly larger than that of the Blasius flow. In particular, for increasing bump height, the spanwise wavelength of the initial vortices increases, so that for the larger bump the initial perturbation is composed of just one pair of vortices in the spanwise direction, which appear to be flatter than the ones observed in the previous cases. One can observe the structure of the initial vortices in Figure 7, which shows the streamlines, as well as the contours of the streamwise component of the perturbation velocity on the plane $x = 77.5$, passing through the center of the bump. For the smaller bump, several alternated vortices are present; between them, regions of alternated streamwise component of the velocity perturbation can be observed. The structure of this perturbation is very similar to the one recovered for the Blasius base flow, although the perturbation is spanwise-localized on top of the roughness element. It is also noteworthy that, as in the case of the boundary layer [11, 17], the streamwise component of the perturbation is the smallest one at initial time, and the spanwise component is the largest. This is also observed for the case of the large bump (the two frames of Figure 7 showing approximately the same values of velocity), although the shape of the perturbation changes. Figure 7 (right frame) shows the presence of only two vortices above the bump, and two smaller ones at its sides. Between them, two zones of strong streamwise perturbation, alternated in the wall-normal direction, can be observed. This structure presents strong differences with respect to the one recovered in the Blasius case, meaning that in the presence of a three-dimensional flow induced by the roughness element, the amplification mechanisms inducing a transient growth in a boundary-layer strongly change.

An insight on such amplification mechanisms can be provided by analyzing the evolution of the initial optimal perturbations at the target time of the optimization. Figures 5 (right) and 8 show the streamwise component of the optimal perturbation at the target time $T = 50$ for the Blasius base flow, the flow past the small and the large bump (from left to right), respectively. For the Blasius flow (right frame of Figure 5), the optimal perturbation is composed of streaky structures alternated in the streamwise and spanwise directions, preserving the same wavelength of the one observed at $t = 0$, although such structures change their streamwise inclination. In fact, the perturbation tilts downstream via the Orr mechanism [36], extracting the energy from the mean shear by conserving the spanwise vorticity [4, 10]. This
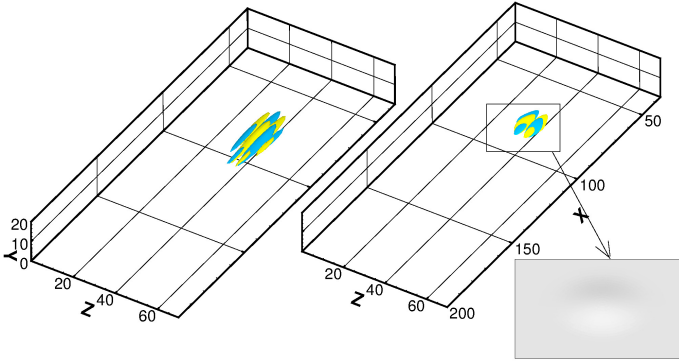
FIGURE 6. Iso-surfaces of the spanwise component of velocity (blue and yellow for negative and positive values, respectively) for the initial optimal perturbations obtained at $T = 50$ for the smallest and the largest bump (from left to right). The inset shows the location and the shape of the roughness element.
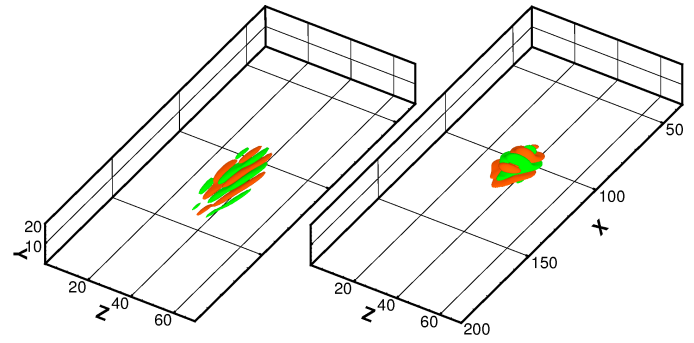

FIGURE 7. Contours of the streamwise component of velocity and streamlines in the plane at $x = 77.5$ for the initial optimal perturbation obtained at $T = 50$ for the smallest and the largest bump (from top to bottom). The spanwise and wall-normal axis are not on the same scale.

non-modal short-term growth mechanism is not the main one to induce an energy amplification in the boundary layer, since the main part of the transient growth is due to the lift-up effect, in which slow/fast fluid is transported upwards/downwards in the boundary layer creating slow/fast streaks of streamwise perturbation and increasing the disturbance energy. Thus, at target time, the optimal perturbation for the Blasius flow results in streaky structures with alternating-sign velocity components in the x di-

FIGURE 8. Iso-surfaces of the streamwise component of velocity (green and red for negative and positive values, respectively) for the optimal perturbations at target time $T = 50$ for the smallest and the largest bump (from left to right).
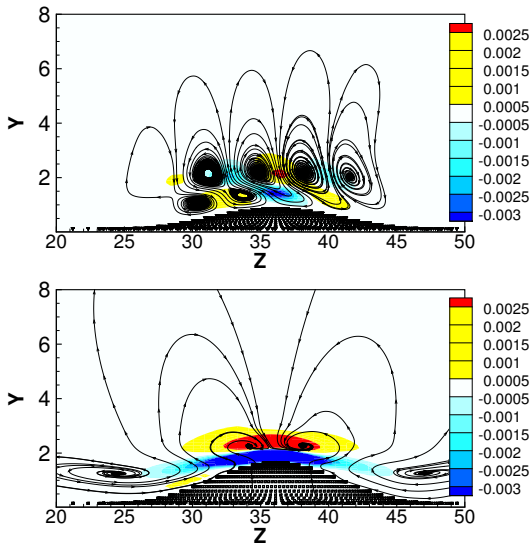
rection, characterized by large values of the streamwise velocity component.

For the case of the small bump, the amplification mechanisms appear to be the same, as one can infer by observing the energy gain curve in Figure 4, as well as the perturbation structure in Figure 8 (left frame). In fact, as in the case of the Blasius flow, the perturbation is composed of streaky structures alternated in the streamwise and spanwise directions, although three main differences can be noticed: i) the perturbation is placed more upstream than in the Blasius case; ii) the perturbation is localized in the spanwise direction in a narrow zone corresponding to the bump location; iii) the vortices are not perfectly aligned with the $x-$axis, presenting a slight inclination with respect to the streamwise direction, and resulting in an arrow-shaped wave packet. These features are due to the three-dimensionality of the flow, which is characterized by a strong wake past the roughness element which deforms the wall-normal shear responsible for the Orr and the lift-up mechanisms. For the small bump, this deformation is weak, so it does not result in a large difference in energy gain, but only in a different inclination of the structures and in a strong localization of the disturbance. The latter is an important feature of the optimal perturbation in the presence of a roughness element, since realistic perturbations in a boundary-layer flow are usually spatially localized. It should be also noticed that, for the same initial energy, a localized perturbation is characterized by larger amplitudes, explaining why the localization is a very important feature of optimal perturbations in a non-linear framework, efficiently inducing by-pass transition in shear flows [34, 37, 38].

For the case of the larger bump, the structure of the perturbation at target time is quite different, being characterized by patches of perturbation velocity with high streamwise component and alternating sign (see the right frame of Figure 8). Such patches do not present a streaky structure, but are characterized
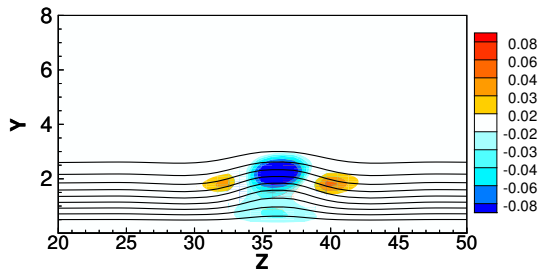
7

FIGURE 9. Contours of the streamwise velocity component of the optimal perturbation at target time $T = 50$ in the plane $x = 112.5$ for the smallest and the largest bump (from top to bottom). The solid contours represents the streamwise component of the base flow velocity in the range $[0.1, 0.9]$. Axis are not on the same scale.

by an "arch" structure at the center of the wave-packet, and an arrow structure at their sides. This perturbation shows a stronger spanwise and streamwise localization with respect to the smaller bump case, and presents a large inclination with respect to the streamwise direction, indicating that the three-dimensionality of the flow is large enough to induce different amplification mechanisms. The difference with respect to the previous case can be better visualized in Figure 9 which shows the streamwise component of velocity of the optimal perturbation (shaded contours) and of the base flow (solid contours) on the plane $x = 112.5$ for the two bumps. For the smaller bump (upper frame) one can

observe spanwise-alternated patches of streamwise perturbation, whereas for the larger one (lower frame) the regions of large streamwise perturbation are alternated also in the wall-normal direction and present a flatter structure. It is noteworthy that, in the latter case, the largest values of the perturbation velocity are recovered in the zones of maximum shear of the underlying streaks. Moreover, one can clearly observe a varicose symmetry (see [4]) with respect to the central negative streaks, which is not recovered in the previous case. One can also notice the much larger values of the streamwise component of velocity for the case of the larger bump, indicating the destabilizing effect of the large amplitude streaks induced by the roughness element. Thus, for the case of the larger bump, the optimal perturbations are very different with respect to the ones recovered by optimization in a Blasius flow; however, it could be observed that they present some similarities with the optimal varicose secondary perturbations of a boundary-layer flow in the presence of saturated parallel streaks, which have been computed in [39] by means of a local optimization method. Similarly to what observed here, the optimal perturbations of a streaky parallel flow have their maximum values at the locations of maximum shear of the underlying streaks, and the streamwise velocity component results to be the most amplified. Thus, we can conjecture that the amplification mechanism which induces a strong increase of the energy growth for the larger bump case is due to a secondary non-normal instability of the streaky base flow; such a secondary non-normal instability cannot arise in the case of the very small amplitude streaks induced by the smaller bump. As described in [39], the energy gain induced by this secondary non-normal instability is due to the transport of the wall-normal shear, operated by the Orr mechanism, and also to the tilting of the mean flow vorticity, associated with the work of the Reynolds stress uw on the spanwise basic shear U_z (as in the streak generation process in two-dimensional flows). This mechanism, which is observed for both the sinuous and the varicose perturbations, is not recovered in the case of the Blasius base flow in a linear framework, and is linked to the three-dimensionality of the base flow.

Similar optimal perturbations are observed for slightly larger values of the target time, up to the optimal time ($T = 100$ for the larger bump); for $T > 100$, the shape of the optimal perturbation for the case of the larger bump changes. Figure 10 provides the iso-surfaces of the spanwise velocity component of the initial optimal perturbations obtained with $T = 200$ for the two roughness elements. For the smaller bump (upper frame), the initial perturbation is still composed of upstream-inclined streamwise vortices alternated in the spanwise direction, although they are more elongated than in the case with a smaller target time. On the other hand, some differences with respect to the optimal solution at smaller target times are observed for the case of the larger bump (lower frame). The spanwise component of the velocity perturbation appears to be symmetric with respect to the plane $x - y$ cutting the bump at its center, whereas at $T = 50$ it was antisym-
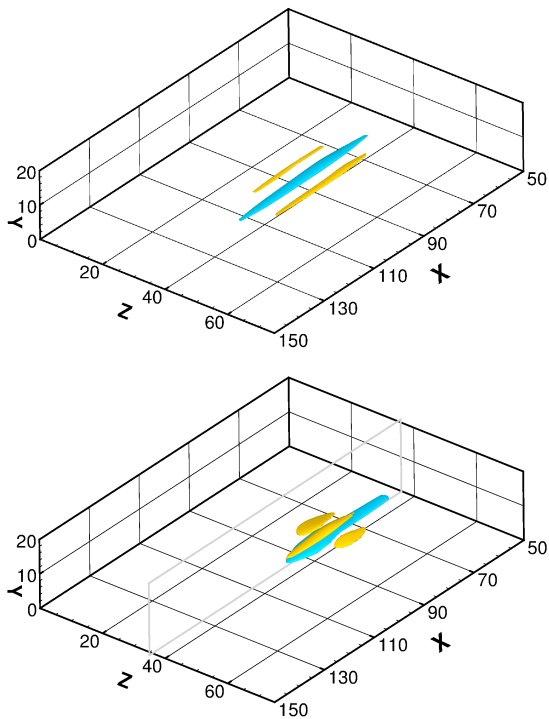
FIGURE 10. Iso-surfaces of the spanwise component of velocity (blue and yellow for negative and positive values, respectively) for the initial optimal perturbations obtained at $T = 200$ for the smallest and the largest bump (from top to bottom).

FIGURE 11. Iso-surfaces of the streamwise component of velocity (green and red for negative and positive values, respectively) for the optimal perturbations at target time $T = 200$ for the smallest and the largest bump (from top to bottom).

metric with respect to this plane (see Figure 6). Moreover, the vortices are more elongated and two of them are alternated also in the wall-normal direction. Also at target time the optimal perturbations for $T = 200$ present some differences with respect to the previous cases. Figure 11 provides the iso-surfaces of the streamwise velocity component of the optimal disturbances at $T = 200$ for the cases of the two bumps. For the case of the smaller bump (upper frame), we observe a wave-packet of elongated streaky structures, alternated only in the spanwise direction, which do not show any inclination with respect to the streamwise direction. This is due to the fact that for the case of the smaller bump, well downstream of the roughness element the flow does not show strong modifications with respect to the Blasius solution (see Figure 3). Thus, the shape of the optimal perturbation is more affected by the three-dimensionality of the flow at smaller target times than at larger ones. A different behavior is observed for the case of the larger bump. For $T = 200$, the optimal perturbation (lower frame of Figure 11) is a Λ−shaped wave-packet composed of spanwise-alternated streaky structures being characterized by a strong inclination with respect to the streamwise direction. The "arch" structures present at smaller target time are not observed, and the streamwise component of the veloc-
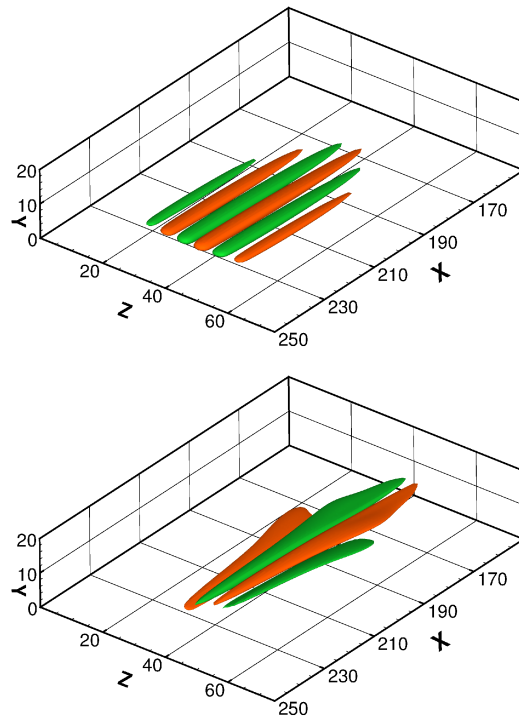
ity perturbation is antisymmetric with respect to the $x - y$ plane cutting the bump at its center, whereas it was symmetric with respect to such a plane for a smaller target time. Thus, it appears that the optimal disturbances obtained for $T > 100$ in the case of the large bump are sinuous perturbations to the streaky flow (see [4]), whereas for $T \leq 100$ we have obtained optimal perturbations characterized by a varicose structure. Such a different shape of the perturbation is linked to the drop of the energy gain observed in Figure 4 for values of the target time between 100 and 150. The differences between the optimal disturbances at "small" ($T \leq 100$) and "large" ($T > 100$) target time can be better observed in Figures 12 and 13 at $t = 0$ and $t = T$, respectively. Figure 12 shows the streamwise velocity component of the initial optimal disturbances obtained for $T = 100$ and $T = 150$, on the plane $x = 77.5$. Despite the fact that the two target times are close to each other, the optimal disturbances change strongly in shape, showing: i) an "arch" structure for $T = 100$, with wall-normal alternated patches of streamwise disturbance characterized by a varicose symmetry, and two vortices on the sides of the bump; ii) a flat structure for $T = 150$, with spanwise-alternated patches of streamwise disturbance characterized by a sinuous symmetry, a main vortex on the top of the bump and two weaker ones
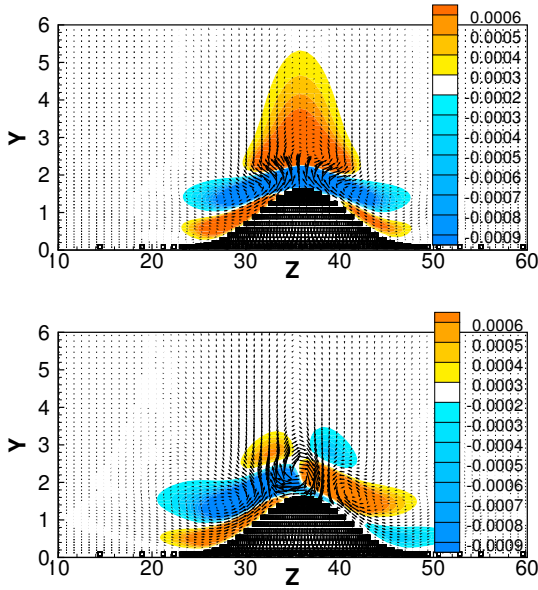
FIGURE 12. Vectors of the spanwise and wall-normal and contours of the streamwise component of velocity in the plane $x = 77.5$ for the initial optimal perturbations obtained with $T = 100$ and $T = 150$ (from top to bottom) for the case of the larger bump.

on its sides. These differences are recovered also at target time, as shown in Figure 13 on two $x-$ constant planes. Indeed, the streamwise component of the optimal disturbance at $T = 100$ (upper frame) maintains its varicose structure, being symmetric with respect to the $z = 36$ plane, whereas for $T = 150$ it keeps a sinuous structure, being antisymmetric with respect to such a plane. However, the two perturbations also present some similarities, since they both have their maximum values on the zones of maximum shear of the base flow, which are represented in the figure by the solid contours of the streamwise component of velocity of the base flow. Moreover, in both cases, the streamwise component of velocity is the most amplified, and its amplitudes are found to be similar both at $t = 0$ and at $t = T$, although the optimal energy gain for $T = 150$ is smaller than the one obtained for $T = 100$. Such features of the optimal disturbances at "small" and "large" target times, as well as their shape, closely recall the varicose and sinuous (respectively) local optimal perturbations found in [39] for a base flow composed of parallel saturated streaks.

Thus, we can conjecture that the amplification mechanisms which induce an optimal growth of the energy for the larger bump case are linked to the secondary non-normal instability of the streaky base flow with respect to varicose perturbations for smaller target times, and sinuous ones for larger target times. Moreover, the highest value of the energy gain is obtained at

10

FIGURE 13. Shaded contours of the streamwise component of the velocity perturbation in the planes $x = 135$ and $x = 165$ (from top to bottom) for the optimal perturbation at target time $T = 100$ and $T = 150$ (from top to bottom) for the case of the larger bump. The solid line represents the streamwise component of the base flow velocity in the range $[0.1, 0.9]$. Axis are not on the same scale.

$T = 100$ for a varicose perturbation, pointing out the importance of varicose instabilities for such a flow. This is a surprising and important result since it disagrees with the well-known result of the secondary asymptotical instability of boundary layer streaks, assessing that the primary instability of a streaky flow is of sinuous type [40]. Such a discrepancy can be explained by observing that the base flow itself is characterized by a varicose symmetry in the near field downstream of the bump, linked to the presence of a large wake, the positive and negative streaky structures showing a finite inclination with respect to the streamwise axis (see the bottom frame of Figure 3). Further downstream, the flow turns into a nearly-parallel streaky flow, since the streaks have a negligible inclination with respect to the $x-$axis. Thus, at small target times the optimal disturbances are strongly affected by such a varicose structure of the base flow, inducing a varicose secondary non-normal instability, whereas they turn into sinuous ones when they reach the nearly parallel streaky flow far from the bump.

Conclusions

This work provides a fully three-dimensional energy optimization analysis, looking for perturbations inducing the largest energy growth at a finite time in a boundary-layer flow in the presence of roughness elements of smooth axisymmetric shape. The analysis aims at describing those three-dimensional amplification mechanisms which by-pass the two-dimensional asymptotical growth of Tollmien–Schlichting waves and lead the flow to a rapid transition. To this purpose, we have coupled the immersed boundary technique, useful to describe complex geometries, with a Lagrangian optimization in a three-dimensional framework. Direct-adjoint optimizations have been performed in order to identify those initial perturbations of the base flow which are able to produce the largest disturbance growth at any given target time. Two smooth roughness elements have been studied, characterized by different height. Even if, for the small bump, the deformation of the base flow is weak, so it does not result in a large difference in energy gain with respect to the Blasius boundary layer, a strong localization of the optimal disturbance is observed. This result indicates that very small irregularities of the wall surface (always present in realistic configurations) may be the cause of the localization of the perturbations which eventually evolve towards turbulent spots in a non-linear framework. For the case of the larger bump, the energy of the perturbations overtakes of one order of magnitude the one observed for a Blasius flow, indicating that the roughness element has a destabilizing effect at finite times due to non-normal effects, even if it is able to stabilize the TS waves (see [24]). Furthermore, for the larger bump, it appears that the optimal disturbances obtained for $T > 100$ are sinuous perturbation, whereas for $T \leq 100$ optimal perturbations are characterized by a varicose structure. Moreover, the highest value of the energy gain is obtained at $T = 100$

for a varicose perturbation, pointing out the importance of varicose instabilities for such a flow. This is a remarkable result since it disagrees with the well-known result of the secondary asymptotical instability theory of boundary layer streaks, assessing that the primary instability of a streaky flow is of sinuous type. The different behavior can be explained by observing that the base flow itself is characterized by a varicose symmetry in the near field downstream of the bump, whereas, at larger abscissae, the flow turns into a nearly-parallel streaky flow. Thus, at small target times the optimal disturbances are strongly affected by such a varicose structure of the base flow, inducing a varicose secondary non-normal instability, whereas they turn into sinuous ones when they reach the nearly parallel streaky flow far from the bump. These results confirm the importance of taking into account the three-dimensionality of the base flow using three-dimensional global instability methods, in order to better understand the most likely scenarios of transition in a boundary-layer flow.

REFERENCES

[1] Marusic, I., 2009. "Unravelling turbulence near walls ". *J. Fluid Mech., 630*, pp. 1–4.

[2] Cutrone, L., De Palma, P., Pascazio, G., and Napolitano, M., 2008. " Predicting transition in two- and three-dimensional separated flows ". *Int. J. Heat Fluid Flow, 29*, pp. 504–526.

[3] Cutrone, L., De Palma, P., Pascazio, G., and Napolitano, M., 2010. "A RANS flamelet-progress-variable method for computing reacting flows of real-gas mixtures ". *Computers and Fluids, 39*, pp. 485–498.

[4] Schmid, P., and Henningson, D., 2001. *Stability and transition in shear fows*. Springer.

[5] Schoppa, W., and Hussain, F., 2002. "Coherent structure generation in near-wall turbulence ". *J. Fluid Mech., 453*, pp. 57–108.

[6] Brandt, L., Schlatter, P., and Henningson, D. S., 2004. "Transition in a boundary layers subject to free-stream turbulence ". *J. Fluid Mech., 517*, pp. 167–198.

[7] Landahl, M. T., 1980. "A note on an algebraic instability of inviscid parallel shear flows ". *J. Fluid Mech., 98*, pp. 243–251.

[8] Landahl, M., 1990. "On sublayer streaks ". *J. Fluid Mech., 212*, pp. 593–614.

[9] Farrell, B., 1988. "Optimal excitation of perturbations in viscous shear flow ". *Phys. Fluids, 31*, pp. 2093–2102.

[10] Butler, K. M., and Farrell, B. F., 1992. "Three-dimensional optimal perturbations in viscous shear flow ". *Phys. Fluids A, 4*, pp. 1637–1650.

[11] Luchini, P., 2000. "Reynolds number indipendent instability of the Blasius boundary layer over a flat surface: optimal perturbations ". *J. Fluid Mech., 404*, pp. 289–309.

[12] Schmid, P. J., 2000. "Linear stability theory and by pass transition in shear flows". *Phys. Plasmas, 7*, pp. 1788–1794.

[13] Corbett, P., and Bottaro, A., 2000. "Optimal perturbations for boundary layers subject to stream-wise pressure gradient". *Phys. Fluids, 12*, pp. 120–130.

[14] Barkley, D., and Henderson, R. D., 1996. "Floquet stability analysis of the periodic wake of a circular cylinder". *J. Fluid Mech, 322*(215–241).

[15] Theofilis, V., Hein, S., and Dallmann, U., 2000. "On the origins of unsteadiness and three dimensionality in a laminar separation bubble". *Phil. Trans. R. Soc. Lond., 358*(1777), pp. 3229–3246.

[16] Ehrenstein, U., and Gallaire, F., 2005. "On two dimensional temporal modes in spatially evolving open flows: the flat-plate boundary layer". *J. Fluid Mech., 536*, pp. 209–218.

[17] Cherubini, S., Robinet, J.-C., Bottaro, A., and De Palma, P., 2010. "Optimal wave packets in a boundary layer and initial phases of a turbulent spot". *J. Fluid Mech., 656*, pp. 231–259.

[18] Acalar, M., and Smith, C., 1987. "A study of hairpin vortices in a laminar boundary layer: part 1, hairpin vortices generated by a hemisphere protuberance". *J. Fluid Mech., 175*, pp. 1–41.

[19] Joslin, R. D., and Grosch, C. E., 1995. "Growth characteristics downstream of a shallow bump: Computation and experiment.". *Phys. Fluids, 7*(12), pp. 3042–3047.

[20] Lipatov, I., and Vinogradov, I., 2000. "Three-dimensional flow near surface distortions for the compensation regime". *Philos. Trans. R. Soc. London A*(358), pp. 3143–3153.

[21] Fransson, J., Brandt, L., Talamelli, A., and Cossu, C., 2004. "Experimental and theoretical investigation of the nonmodal growth of steady streaks in a flat plate boundary layer". *Phys. Fluids, 16*(10), pp. 3627–3638.

[22] Choudhari, M., and Fischer, P., 2005. "Roughness-induced transient growth, AIAA-2005-4765, 35th AIAA Fluid Dynamics Conference and Exhibit, Toronto, Ontario Canada.". *35th AIAA Fluid Dynamics Conference and Exhibit, Toronto, Ontario Canada, AIAA-2005-4765*.

[23] Fransson, J., Talamelli, A., Brandt, L., and Cossu, C., 2006. "Delaying transition to turbulence by a passive mechanism". *Phys. Rev. Lett., 96*(6), p. 064501.

[24] Piot, E., Casalis, G., and Rist, U., 2008. "Stability of the laminar boundary layer flow encountering a row of roughness elements: Biglobal stability approach and dns". *European Journal of Mechanics - B/Fluids, 27*(6), pp. 684–706.

[25] Giannetti, F., and Luchini, P., 2007. "Structural sensitivity of the first instability of the cylinder wake". *J. Fluid Mech., 581*, pp. 167–197.

[26] Bottaro, A., 1990. "Note on open boundary conditions for elliptic flows". *Num. Heat Transfer B, 18*, pp. 243–256.

[27] Verzicco, R., and Orlandi, P., 1996. "A finite-difference scheme for the three-dimensional incompressible flows in cylindrical coordinates". *J. Comp. Phys., 123*(2), pp. 402–414.

[28] O'Rourke, J., 1993. *Computational Geometry in C*. Cambridge Univ. Press.

[29] Mohd-Yusof, J., 1997. *Combined immersed boundaries/B-splines methods for simulations of flows in complex geometries*. CTR Annual Research Briefs, NASA Ames/Stanford University.

[30] Fadlun, E. A., Verzicco, R., Orlandi, P., and Mohd-Yusof, J., 2000. "Combined immersed-boundary finite-difference methods for three-dimensional complex flow simulations". *J. Comput. Phys., 161*, p. 35.

[31] Zuccher, S., Luchini, P., and Bottaro, A., 2004. "Algebraic growth in a blasius boundary layer: optimal and robust control by mean suction in the nonlinear regime". *Eur. J. Mech. B/Fluids, 513*, pp. 135–160.

[32] Marquet, O., Sipp, D., Chomaz, J.-M., and Jacquin, L., 2008. "Amplifier and resonator dynamics of a low-Reynolds-number recirculation bubble in a global framework". *J. Fluid Mech., 605*, pp. 429–443.

[33] Polak, E., and Ribière, G., 1969. "Note sur la convergence de directions conjuguées". *Rev. Francaise Informat Recherche Operationnelle, 16*, pp. 35–43.

[34] Cherubini, S., De Palma, P., Robinet, J.-C., and Bottaro, A., 2010. "Rapid path to transition via nonlinear localized optimal perturbations". *Phys. Rev. E, 82*, p. 066302.

[35] Monokrousos, A., Akervik, E., Brandt, L., and Henningson, D. S., 2010. "Global three-dimensional optimal disturbances in the Blasius boundary-layer flow using time-steppers". *J. Fluid Mech., 650*, pp. 181–214.

[36] Orr, W. M., 1907. "The stability or instability of the steady motions of a liquid. Part I". *Proceedings of the Royal Irish Academy, A, 27*, pp. 9–68.

[37] Pringle, C. C. T., and Kerswell, R., 2010. "Using nonlinear transient growth to construct the minimal seed for shear flow turbulence". *Phys. Rev. Lett., 105*, p. 154502.

[38] Monokrousos, A., Bottaro, A., Brandt, L., Di Vita, A., and Henningson, D. S., 2011. "Non-equilibrium thermodynamics and the optimal path to turbulence in shear flows". *Phys. Rev. Lett., 106*, p. 134502.

[39] Hoepffner, J., Brandt, L., and Henningson, D. S., 2005. "Transient growth on boundary layer streaks". *J. Fluid Mech., 537*, pp. 91–100.

[40] Andersson, P., Brandt, L., Bottaro, A., and Henningson, D. S., 2001. "On the breakdown of boundary layer streaks". *J. Fluid Mech., 428*, pp. 29–60.